


**Impact of coordinate frames on mode formation in twisted waveguides**Johannes Bürger <sup>\*</sup>*Chair in Hybrid Nanosystems, Nanoinstitut Munich, Ludwig-Maximilians-Universität Munich, Königinstraße 10, 80539 Munich, Germany*Adrià Canós Valero *Institute of Physics, University of Graz, Universitätsplatz 5, 8010 Graz, Austria*Thomas Weiss *Institute of Physics, University of Graz, Universitätsplatz 5, 8010 Graz, Austria  
and 4th Physics Institute and SCoPE, University of Stuttgart, Pfaffenwaldring 57, 70569 Stuttgart, Germany*Stefan A. Maier *School of Physics and Astronomy, Monash University, Clayton, Victoria 3800, Australia;  
Chair in Hybrid Nanosystems, Nanoinstitut Munich, Ludwig-Maximilians-Universität Munich, Königinstraße 10, 80539 Munich, Germany;  
and The Blackett Laboratory, Department of Physics, Imperial College London, London SW7 2AZ, United Kingdom*Markus A. Schmidt *Leibniz Institute of Photonic Technology, Albert-Einstein-Str. 9, 07745 Jena, Germany;  
Otto Schott Institute of Materials Research (OSIM), Friedrich-Schiller-Universität Jena, Fraunhoferstr. 6, 07743 Jena, Germany;  
and Abbe Center of Photonics and Faculty of Physics, Friedrich-Schiller-Universität Jena, Max-Wien-Platz 1, 07743 Jena, Germany*

(Received 24 November 2023; revised 14 March 2024; accepted 15 March 2024; published 5 April 2024)

Off-axis twisted waveguides possess unique optical properties such as circular and orbital angular momentum (OAM) birefringence, setting them apart from their straight counterparts. Analyzing mode formation in such helical waveguides relies on the use of specific coordinate frames that follow the twist of the structure. In this paper, the differences between modes forming in high-contrast off-axis twisted waveguides defined in the three most important coordinate systems—the Frenet-Serret, the helicoidal, or the Overfelt frame—are investigated through numerical simulations. We explore modal characteristics up to high twist rates (pitch: 50  $\mu\text{m}$ ) and clarify a transformation allowing us to map the modal fields and the effective index back to the laboratory frame. In case the waveguide is single-mode, the fundamental modes of the three types of waveguides show significant differences in terms of birefringence, propagation loss, and polarization. Conversely, the modal characteristics of the investigated waveguides are comparable in the multimode domain. Furthermore, our paper examines the impact of twisting on spatial mode properties. At high twist rates, a separation of modes with different spins is observed, suggesting a potential influence of the photonic spin Hall effect. Additionally, twisting induces OAM-dependent changes in the intensity distribution, indicating the presence of the photonic orbital Hall effect. Lastly, modes of single-mode helical waveguides were found to exhibit superchiral fields on their surfaces. These findings provide a comprehensive basis for further research into the physics of twisted off-axis waveguides. Implementation approaches such as 3D nanoprining or fiber-preform twisting open the doors to potential applications of such highly twisted waveguides, including chip-integrated devices for broadband spin- and OAM-preserving optical signal transport, as well as applications in chiral spectroscopy or nonlinear frequency conversion.

DOI: [10.1103/PhysRevB.109.165301](https://doi.org/10.1103/PhysRevB.109.165301)**I. INTRODUCTION**

The interest in off-axis twisted waveguides started emerging in the 1980s due to the observation that single-mode fibers helically coiled around a cylinder exhibit circular birefringence, manifested by the rotation of the polarization state of linearly polarized light as it propagates along the waveguide [1–4]. The rotation can be understood based on the transver-

sality of light [1], which means that the polarization vector is constrained to the surface of the  $\mathbf{k}$  sphere. As the wave vector  $\mathbf{k}$  changes directions when light propagates along the helix, the polarization vector is parallel transported on the surface of the sphere [5]—a concept well-known from differential geometry [6]. Due to the curvature of this surface, it was found that the polarization vector does not necessarily return to its original state after the light completes a closed loop on the  $\mathbf{k}$  sphere. More specifically, the polarization vector rotates relative to the laboratory frame whenever the light's trajectory features a nonzero torsion (which refers to a purely

<sup>\*</sup>j.buerger@physik.uni-muenchen.de

geometrical quantity and is not related to any torsional stress in the material). This conceptual framework initially served well in explaining the observed circular birefringence in helical fibers.

The theory evolved further in the years thereafter, in particular, it was realized that light traveling along curved trajectories experiences a spin-orbit and an orbit-orbit interaction coupling the spin or orbital angular momentum (OAM) of a beam of light to its orbital motion [5,7–9]. The emergence of circular and OAM birefringence in helically coiled fibers could now be explained as a direct consequence of these couplings. Conversely, spin-orbit and orbit-orbit interactions were found to act back on the trajectory of light splitting the beam depending on its spin and OAM. These effects are now known as the photonic spin Hall [9,10] and orbital Hall effects [8,11].

From an applied perspective, helical waveguides were mostly used for their circular birefringence, which prevents linearly polarized light from becoming elliptically polarized in the presence of mechanical stress. This robustness against environmental fluctuations is employed in applications such as fiber optic current and magnetic field sensors based on the Faraday effect [12–14] or optical twist and tension sensors [1].

In all of these early works, the cross-sectional shape of the helical waveguides is assumed to be circular in the plane perpendicular to the helical path, which can be well described in the Frenet-Serret coordinate system. On the other hand, more recent experimental works often use the helicoidal coordinate system to investigate fibers containing off-axis twisted cladding elements [15–19]. However, little attention has been paid to the fact that the geometry of helical waveguides defined in these two coordinate systems is, in general, different, which can impact their optical properties.

In this paper, we present an in-depth analysis of the differences between the two coordinate frames in defining helical waveguides and show that the resulting geometries only agree at low twist rates. Furthermore, we compare the results to helical waveguides defined in a third coordinate frame, the Overfelt frame [20], which is derived from a toroidal geometry. Note that we always use the term “helical waveguide” to refer to an off-axis twisted waveguide, in distinction to on-axis twisted waveguides [21–24] or two-dimensional spiraling waveguides [25–27].

Another aspect frequently lacking in previous works is a comprehensive description of the transformation of fields from the helicoidal frame back to the laboratory frame. In this paper, we describe this process in detail and explain under which conditions it is possible to define an effective refractive index for modes of on- and off-axis twisted waveguides in the laboratory frame. Such an effective index is needed, for example, when analyzing coupling to modes in straight waveguides or for comparison to experimental results.

We conducted simulations for both single-mode and multi-mode variants of the three off-axis twisted waveguide types and compared the results to an analytical model for the effective index [28] and loss [29] of modes in helical waveguides. The paper investigates twist rates of up to 20 turns per mm, which are, to our knowledge, the highest investigated so far for off-axis twisted waveguides (an overview of such works can be found in Table SI of the Supplemen-

tal Material [30]). Spin- and OAM-dependent splittings in the spatial properties of the modes were analyzed, as well as the emergence of superchiral fields on the surface of the waveguides (i.e., fields with a larger chiral asymmetry than circularly polarized plane waves [31,32]).

All simulations were performed for high-index contrast waveguides based on the general motivation that helical waveguides can be fabricated with such parameters using 3D nanoprinting (two-photon polymerization) [33].

## II. RESULTS

### A. Coordinate systems for helical waveguides

First, we present three common coordinate systems that can be used to define waveguides that are invariant along a helical path. Throughout this paper, all investigated helices are left-handed, i.e., the waveguides are attached to the following path  $\mathbf{c}(z)$ :

$$\mathbf{c}(z) = \begin{pmatrix} \rho \cos(\alpha z) \\ -\rho \sin(\alpha z) \\ z \end{pmatrix}, \quad (1)$$

where  $\alpha = 2\pi/P$  is the angular twist rate,  $P$  is the pitch of the helix, and  $\rho$  its radius. We refer to  $1/P$  as the twist rate (number of turns per unit length). Such a helical path is characterized by a constant curvature  $\bar{\kappa} = \rho/(\rho^2 + \alpha^{-2}) > 0$  and torsion  $\tau = -\alpha^{-1}/(\rho^2 + \alpha^{-2})$  explained in more detail in Sec. SIII A 1 of the Supplemental Material [30]. For a left-handed helix,  $\alpha > 0$  and  $\tau < 0$ . To define a helical waveguide, this one-dimensional curve needs to be extended to three dimensions. To achieve this, the first step is to establish a suitable coordinate system.

#### 1. Frenet-Serret frame

The most natural choice for a coordinate system given any curve  $\mathbf{c}(z)$  is the Frenet-Serret frame, a local orthonormal right-handed coordinate system that is attached to the curve. Its unit vectors are the tangent vector  $\hat{\mathbf{T}}$  of the curve, the normal vector  $\hat{\mathbf{N}}$  pointing along the derivative of the tangent, and the binormal vector  $\hat{\mathbf{B}}$  which is orthogonal to  $\hat{\mathbf{T}}$  and  $\hat{\mathbf{N}}$  [34]. For the left-handed helix above, these unit vectors are

$$\hat{\mathbf{T}} = \frac{1}{\sqrt{1 + (\alpha\rho)^2}} \begin{pmatrix} -\alpha\rho \sin(\alpha z) \\ -\alpha\rho \cos(\alpha z) \\ 1 \end{pmatrix}, \quad \hat{\mathbf{N}} = \begin{pmatrix} -\cos(\alpha z) \\ \sin(\alpha z) \\ 0 \end{pmatrix},$$

$$\hat{\mathbf{B}} = \frac{1}{\sqrt{1 + (\alpha\rho)^2}} \begin{pmatrix} -\sin(\alpha z) \\ -\cos(\alpha z) \\ -\alpha\rho \end{pmatrix}. \quad (2)$$

In this form,  $z$  is the only coordinate, while extensions of the Frenet-Serret frame for a ring of helical waveguides with an additional azimuthal coordinate exist [35]. The Frenet-Serret frame will prove to be the best choice to describe off-axis twisted waveguides since the wavefronts of the modes lie within the NB plane (spanned by  $\hat{\mathbf{N}}$  and  $\hat{\mathbf{B}}$ ), as revealed later in Sec. II E 2 ff. The simplest helical waveguide that can be defined in this coordinate system has a circular cross section of radius  $r_c$  in the NB plane and is extended infinitely along the T direction. We refer to such a waveguide as a

Frenet-Serret waveguide, with related content being depicted in green throughout the paper.

## 2. Helicoidal frame

The helicoidal frame is another coordinate system widely used to describe twisted waveguides. Helicoidal coordinates  $(\xi_1, \xi_2, \xi_3)$  are related to the Cartesian coordinates  $(x, y, z)$  via [36]

$$\mathbf{r} = (x, y, z) = (\xi_1 \cos(\alpha \xi_3) + \xi_2 \sin(\alpha \xi_3), -\xi_1 \sin(\alpha \xi_3) + \xi_2 \cos(\alpha \xi_3), \xi_3). \quad (3)$$

For fixed values  $\xi_1$  and  $\xi_2$ , the curve  $\mathbf{r}(\xi_3)$  is a left-handed helix for  $\alpha > 0$ . The basis vectors  $\xi_1$  and  $\xi_2$  of the helicoidal frame lie in the  $xy$  plane while  $\xi_3$  points along the tangent of the helix:

$$\xi_1 = \frac{\partial \mathbf{r}}{\partial \xi_1} = \begin{pmatrix} \cos(\alpha \xi_3) \\ -\sin(\alpha \xi_3) \\ 0 \end{pmatrix}, \quad \xi_2 = \frac{\partial \mathbf{r}}{\partial \xi_2} = \begin{pmatrix} \sin(\alpha \xi_3) \\ \cos(\alpha \xi_3) \\ 0 \end{pmatrix},$$

$$\xi_3 = \frac{\partial \mathbf{r}}{\partial \xi_3} = \begin{pmatrix} -\xi_1 \alpha \sin(\alpha \xi_3) + \xi_2 \alpha \cos(\alpha \xi_3) \\ -\xi_1 \alpha \cos(\alpha \xi_3) - \xi_2 \alpha \sin(\alpha \xi_3) \\ 1 \end{pmatrix}. \quad (4)$$

Therefore, the helicoidal coordinate system is not orthogonal. Similar to before, we define a helicoidal waveguide as having a circular cross section of radius  $r_c$  in the  $\xi_1 \xi_2$  plane and extending infinitely along  $\xi_3$ . Results relating to helicoidal waveguides are depicted in purple. Note that the helicoidal

coordinate system is especially useful if the wavefronts are perpendicular to the  $z$  axis, which usually applies to on-axis twisted waveguides [16,19].

## 3. Overfelt frame

A third coordinate system in which a helical structure is translationally invariant along one axis is the coordinate frame  $(\rho, \phi, \zeta)$  used by Overfelt, here referred to as the Overfelt frame [20]. It is an extension of the toroidal coordinate system along the  $z$  axis with its coordinates being defined as

$$\mathbf{r} = (x, y, z) = (\rho \cos(\phi), \rho \sin(\phi), \zeta + \phi/\alpha). \quad (5)$$

When fixing a particular value of  $\rho$  and  $\zeta$ ,  $\mathbf{r}(\phi)$  describes a left-handed helix for  $\alpha < 0$ . To construct a helical waveguide, a refractive index profile  $n$  is defined in the  $\rho \zeta$  plane (which is identical to the  $\rho z$  plane of a cylindrical coordinate system) and extended infinitely along the  $\phi$  coordinate. When this profile is a circle of radius  $r_c$ , we refer to the resulting structure as an Overfelt waveguide, depicted in blue throughout this paper. Note that the Overfelt system is not orthogonal:

$$\mathbf{e}_\rho = \frac{\partial \mathbf{r}}{\partial \rho} = \begin{pmatrix} \cos(\phi) \\ \sin(\phi) \\ 0 \end{pmatrix}, \quad \mathbf{e}_\phi = \frac{\partial \mathbf{r}}{\partial \phi} = \frac{1}{\alpha} \begin{pmatrix} -\alpha \rho \sin(\phi) \\ \alpha \rho \cos(\phi) \\ 1 \end{pmatrix},$$

$$\mathbf{e}_\zeta = \frac{\partial \mathbf{r}}{\partial \zeta} = \begin{pmatrix} 0 \\ 0 \\ 1 \end{pmatrix}. \quad (6)$$

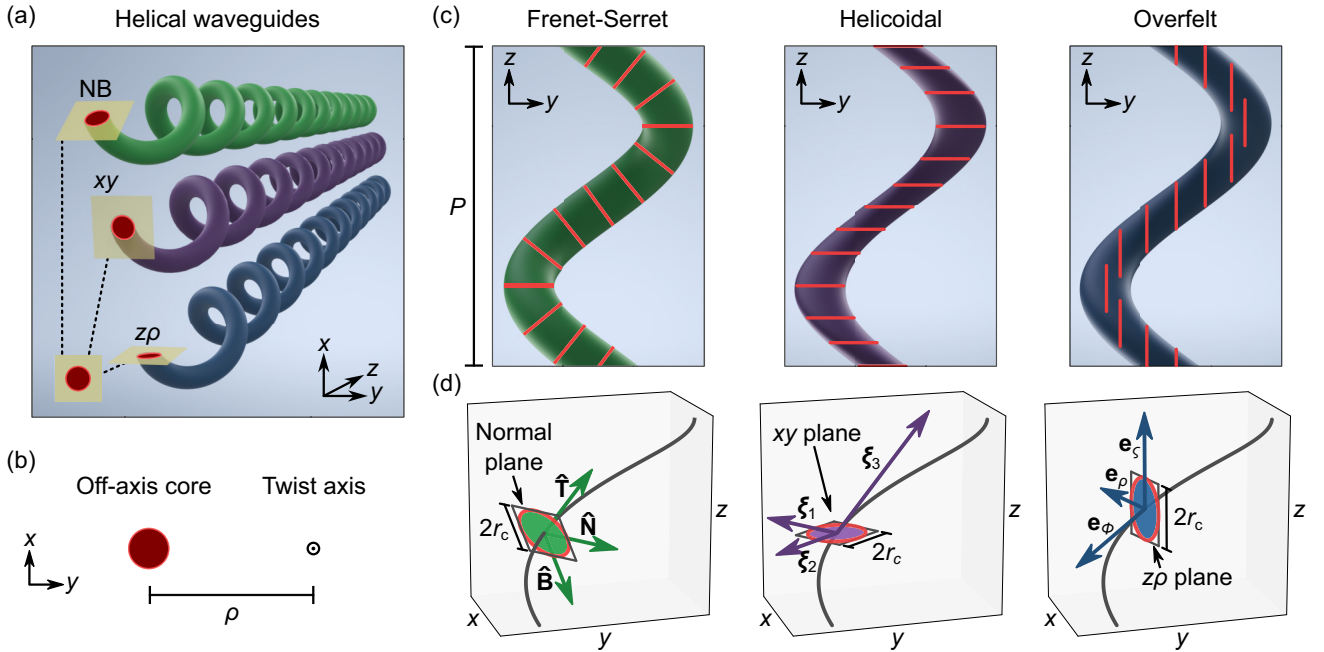


FIG. 1. Helical waveguide geometries. (a) Illustration of the three waveguide types investigated in this paper. (b) In these off-axis twisted waveguides, the core is located at a distance  $\rho$  from the twist axis. (c) Orthographic side views of the Frenet-Serret waveguide (green), the helicoidal waveguide (purple), and the Overfelt waveguide (blue). All helices are left-handed with a pitch distance  $P$ . (d) Basis vectors of the corresponding coordinate systems. The waveguides are defined to have a circular cross section with radius  $r_c$  in the plane spanned by the two basis vectors which are not tangential to the helical path (black curve). Red lines in (c) denote the orientation of the circular cross section. Note that only the Frenet-Serret system is orthogonal.

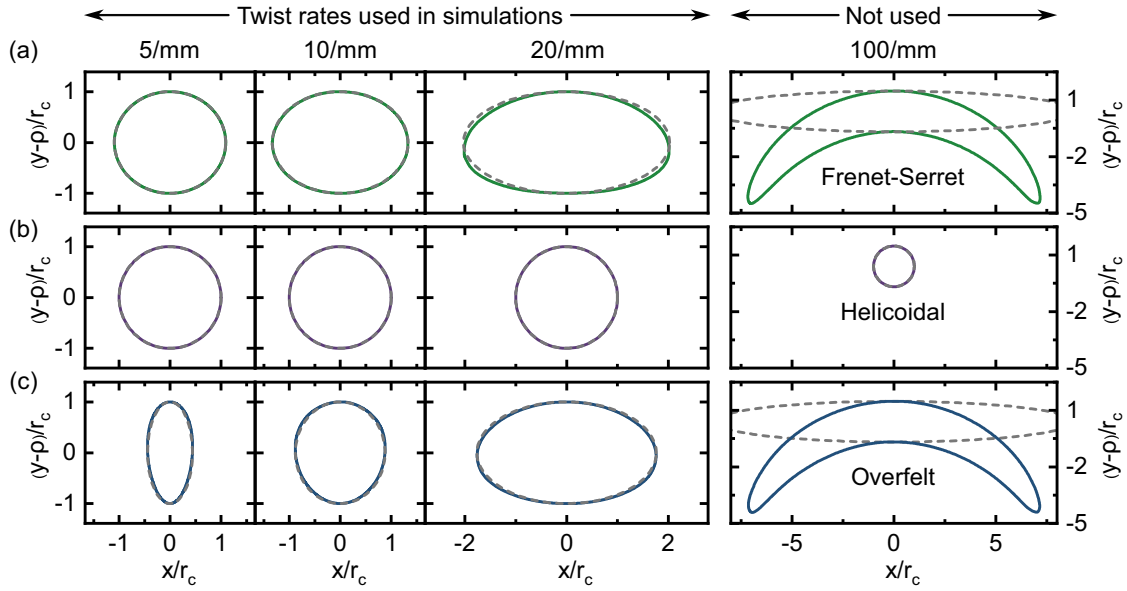


FIG. 2. Cross sections of the helical waveguides in the  $xy$  plane. Cross sections were calculated numerically for four different twist rates (noted on the top) using an off-axis distance of  $\rho = 14 \mu\text{m}$  and  $r_c = 1.8 \mu\text{m}$ . The center of the twist axis is located below the shown coordinate range at  $x = y = 0$ . The geometry of the Frenet-Serret waveguide (green) approaches that of the helicoidal waveguide (purple) for low twist rates and that of the Overfelt waveguide (blue) for high twist rates. Gray dashed lines show an analytical approximation of the cross section, which is valid in the limit of weak coiling ( $\bar{\kappa}r_c \ll 1$ ) and if the extent of the ellipse in the  $x$  direction is much smaller than  $2\pi\rho$ . Waveguide modes were simulated for twist rates up to 20/mm.

More detailed descriptions of the coordinate systems can be found in Sec. SIII of the Supplemental Material [30]. Their basis vectors and the corresponding waveguides are shown in Fig. 1.

### B. Waveguide cross sections in $xy$ plane

To compare the optical properties of the three helical waveguides, mode simulations are conducted using a commercial finite element method (FEM) solver (Propagating-Mode module of JCMwave). JCMwave offers built-in support for the helicoidal coordinate system, along with appropriately defined perfectly matched layers (PMLs). Application of the helicoidal coordinate system requires knowledge of the cross sections of the waveguides in the  $xy$  plane, which are shown for different twist rates in Fig. 2. In the limit of weak coiling, i.e., if the radius of curvature of the helix is much larger than the radius of the core ( $\bar{\kappa}r_c \ll 1$ ), the waveguide can be unrolled onto a plane, allowing the cross sections to be described as ellipses (gray dashed lines in Fig. 2). This process is explained in more detail in Sec. SIV of the Supplemental Material [30]. For the reader's convenience, the formulas for the semiaxes  $r_c^x$  and  $r_c^y$  of the resulting ellipses are shown in Table I.

TABLE I. Semimajor and semiminor axes of the elliptical  $xy$  cross sections of the three helical waveguides in the limit of weak coiling ( $\bar{\kappa}r_c \ll 1$ ) and  $2r_c^x \ll 2\pi\rho$ .

Semiaxis	Frenet-Serret	Helicoidal	Overfelt
$r_c^x$	$\sqrt{1 + (\alpha\rho)^2} r_c$	$r_c$	$\alpha\rho r_c$
$r_c^y$	$r_c$	$r_c$	$r_c$

With the parameters used in this paper, the weak coiling approximation is valid for all investigated waveguides up to arbitrary twist rates ( $\bar{\kappa}r_c < r_c/\rho < 0.13 \ll 1$ ). However, at very high twist rates, the condition  $2r_c^x \ll 2\pi\rho$  needs to be fulfilled as well since the ellipses would otherwise need to be curved, as shown for an extreme twist rate of 100/mm in Fig. 2. The approximation therefore works best for small core radii. In this paper, we simulated waveguides up to twist rates of 20/mm, where  $2r_c^x < 7.3 \mu\text{m} \ll 2\pi\rho \approx 88.0 \mu\text{m}$ , such that the approximation of the cross sections as ellipses is justified.

### C. Transformation of effective index to laboratory frame

The results returned by the solver are the modal fields in the  $xy$  plane at  $z = 0$  and the effective index  $n_{\text{eff}}^{\text{helicoidal}}$  such that the fields  $\tilde{\mathbf{F}}$  in the helicoidal coordinate system satisfy [37]

$$\tilde{\mathbf{F}}(\xi_1, \xi_2, \xi_3) = e^{ik\xi_3 n_{\text{eff}}^{\text{helicoidal}}} \mathbf{F}(\xi_1, \xi_2). \quad (7)$$

We apply a coordinate transformation to evaluate the fields in Cartesian coordinates at  $z \neq 0$ , which subsequently allows us to display all modal quantities within the NB plane. Step-by-step instructions are available in Sec. SV of the Supplemental Material [30].

When transforming the fields to Cartesian coordinates, the fields develop an additional  $z$ -dependent phase factor which we refer to as the transformation phase (cf. Sec. SV A 1 ff. of the Supplemental Material [30]). We show that the transformation phase only increases linearly in  $z$  under specific conditions. Most importantly, the following conditions have to be satisfied: (1) the electric field is circularly polarized with spin  $s = \pm 1$ , and (2) its spatial phase profile is flat or has an OAM profile with an  $e^{il\phi}$  phase dependence. In this case,

it is possible to define an effective index  $n_{\text{eff}}^{\text{lab}}$ , such that the phase of the fields measured in the laboratory frame increases as  $e^{ikz n_{\text{eff}}^{\text{lab}}}$  with

$$n_{\text{eff}}^{\text{lab}} = n_{\text{eff}}^{\text{helical}} + (s + l) \frac{\alpha \lambda}{2\pi}. \quad (8)$$

This equation holds both for off-axis twisted waveguides and on-axis twisted waveguides and matches with earlier derivations valid for on-axis twisted waveguides [37] and off-axis twisted waveguides [28] that were derived based on different approaches. Compared to these earlier derivations, we can also treat cases where the modes feature a noncircular polarization state and find that the transformation phase does not increase linearly in  $z$  in this case. More intuitively, these phase changes are caused by the rotation of the polarization ellipse, following the twist of the waveguide. For example, if the short axis of the polarization ellipse points along the  $x$  direction at  $z = 0$ , it will point along the  $y$  direction at  $z = P/4$ . This effect is unique to modes in twisted waveguides as the polarization state of an eigenmode in a straight waveguide does not change during propagation. The definition of an effective index in the laboratory frame for such elliptically polarized modes might therefore give the wrong impression, that they could couple to a mode in a straight waveguide with the same effective index. Keeping these caveats in mind, we still apply Eq. (8) to all results for better comparability.

#### D. Analytical description of the effective index of Frenet-Serret waveguides

Helical waveguides of the Frenet-Serret type have been studied since the 1980s and a thorough theoretical model has been developed by Alexeyev and Yavorsky based on perturbation theory in 2008 [28]. The model is valid under four conditions: (1) the waveguide is weakly coiled ( $r_c \bar{\kappa} \ll 1$ ), (2) the fields are transverse in the Frenet-Serret frame (scalar wave approximation), (3) the torsion  $\tau$  of the helix can be treated as the small parameter in perturbation theory, and (4) the fields are circularly polarized and possess an OAM phase profile with topological charge  $l$ . In this case, the propagation constant of modes calculated within the Frenet-Serret coordinate frame is changed from that of the straight waveguide by  $\Delta\beta^{\text{Frenet}} = (s + l)\tau$  [28]. In the laboratory frame, the effective mode index can then be approximated as (see derivation in Sec. SVI of the Supplemental Material [30])

$$n_{\text{eff}}^{\text{lab}} = \underbrace{n_0 \sqrt{1 + \alpha^2 \rho^2}}_{\text{Geometric increase in path length}} + \underbrace{(s + l) \frac{\alpha}{k_0} \left( 1 - \frac{1}{\sqrt{1 + \alpha^2 \rho^2}} \right)}_{\text{Spin-orbit (s) and orbit-orbit (l) interaction}}. \quad (9)$$

For small twist rates  $\alpha\rho \ll 1$  the result can be simplified, showing that the splitting of modes with different total angular momentum (TAM) increases strongly with twist rate and helix radius:

$$n_{\text{eff}}^{\text{lab}} = n_0 \sqrt{1 + \alpha^2 \rho^2} + (s + l) \frac{\rho^2 \alpha^3 \lambda}{4\pi} \quad \text{for } \alpha\rho \ll 1. \quad (10)$$

Their result shows that twisting a waveguide lifts the degeneracy between modes with the same magnitude of TAM but different signs. In straight step-index fibers, these modes

are degenerate and therefore the spin and OAM state is not conserved during propagation (minor imperfections in any real-world waveguide lead to a coupling of the degenerate modes).

The birefringence caused by the helical path can also be derived on a more fundamental basis, using the semigeometrical optics approximation [5,7]. Using this approximation, the motion of a wave packet on scales much larger than the wavelength is influenced by spin-orbit and orbit-orbit interactions of light [8,11] (for more details see Secs. SVI A and SIX of the Supplemental Material [30]). These interactions result in the modes of helical waveguides acquiring a spin- and OAM-dependent Berry phase [5,8,38], given by the observation that light traces out a closed loop in  $k$  space as it propagates through one turn of the helix. The solid angle  $\Omega$  that this loop encloses determines the Berry phase as  $\Phi_B = (s + l)\Omega$  and results in the same birefringence term stated in Eq. (9) for the laboratory frame. Notably, the observation of circular birefringence in helically coiled fibers constitutes the first experimental confirmation of Michael Berry's theoretically predicted geometrical phase factor [38–40].

### E. Simulation results for optical properties of helical waveguide geometries

#### 1. Parameters of multimode waveguides

With these preparations, we start analyzing the twist-rate-dependent optical properties of multimode variants of the three waveguides. Based on a recent realization of 3D-nanoprinted helical waveguides [33] and related work on 3D-nanoprinted hollow-core waveguides [41–43], realistic parameters for this fabrication technique were chosen. In particular,  $r_c = 1.8 \mu\text{m}$ ,  $\lambda = 770 \text{ nm}$ , and a refractive index of the core of  $n_{\text{co}} = 1.5423$  with a cladding made out of air ( $V$  number: 17.25, number of guided modes:  $V^2/2 \approx 149$ ). These values correspond to a commonly used photoresist at this wavelength (IP-Dip, Nanoscribe GmbH).

#### 2. Fundamental modes in multimode waveguides

The optical properties of the twisted multimode waveguides are very similar across a large range of investigated twist rates (5/mm–20/mm) since the cross sections of the waveguides are so wide that the specific shape plays a minor role. The two fundamental modes are circularly polarized with the wavefronts lying in the NB plane as shown in Figs. S13 and S14 of the Supplemental Material [30].

The real part of the effective index and the circular birefringence (difference in the real part of the effective index between the LCP and RCP mode, evaluated in the laboratory frame) match very well with the analytical model of Eq. (9) for all waveguide types. Off-axis twisting has two immediate consequences: (1) the effective index of the mode increases due to the longer path that the light is traveling along the helix to reach a certain distance  $z$  [first term in Eq. (9) and Fig. 3(a)] and (2) a splitting occurs between modes with different TAM [second term in Eq. (9) and Fig. 3(b)]. Compared to typical values of birefringence found in polarization-maintaining fibers ( $10^{-3}$ - $10^{-4}$ ), much higher birefringence on the order of

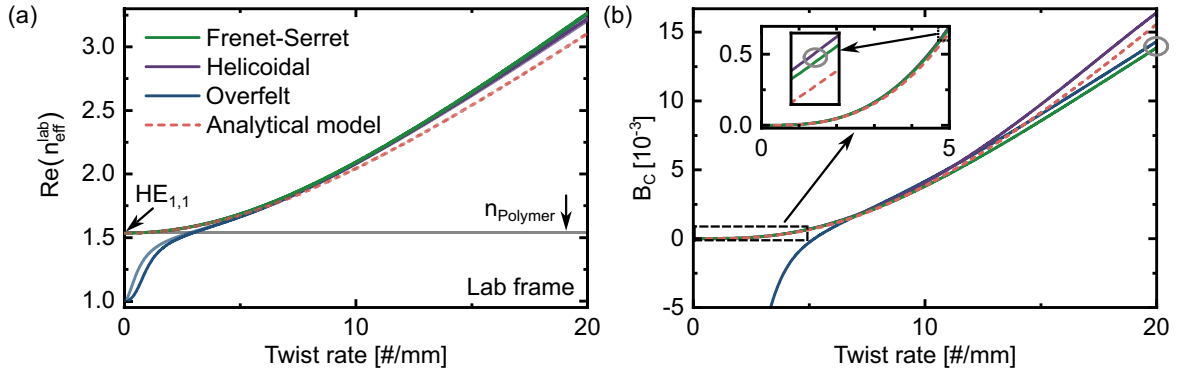


FIG. 3. Optical properties of multimode helical waveguides ( $r_c = 1.8 \mu\text{m}$ ). (a) Twist rate dependence of the real part of the effective mode index of the two fundamental modes calculated in the laboratory frame. A darker color shade denotes the LCP mode, a lighter shade the RCP mode. (b) Circular birefringence  $B_C$  (i.e., difference between the effective index of the two lowest-order modes). Note that for low twist rates ( $< 5/\text{mm}$ ) the modes of the Overfelt waveguide become elliptically polarized. Red dashed lines in (a) and (b) represent an analytical prediction for the Frenet-Serret waveguide [Eq. (9)].

$10^{-2}$  can be reached at the highest investigated twist rate of  $20/\text{mm}$  ( $\alpha\rho = 1.8$ ).

Since the cross section of the Overfelt waveguide becomes infinitely narrow along the B direction for  $\alpha \rightarrow 0$  (see Fig. S14 of the Supplemental Material [30]), its optical properties deviate from those of the other two waveguides for twist rates below  $5/\text{mm}$ . Due to the narrowing of the cross section, the two fundamental modes change from being circularly polarized to linearly polarized at low twist rates, resulting in a larger (linear) birefringence. As the modes are more and more localized in air, the effective index approaches 1 for  $\alpha \rightarrow 0$ .

### 3. OAM modes in multimode waveguides

Next, we investigated the four OAM modes with  $|l| = 6$  in the multimode Frenet-Serret waveguide. The modes are organized in two groups, one originating from the  $\text{EH}_{5,1}$  mode pair of the untwisted waveguide with a TAM of  $\pm 5$  and the other one from the  $\text{HE}_{7,1}$  mode pair with a TAM of  $\pm 7$  [44]. As the twist rate rises, the effective index of the modes overall increases with the same geometrical factor as the fundamental modes [first term in Eq. (9) and Fig. 4(a)]. On the other hand, the birefringence within each mode pair is 5 or 7 times larger than for the fundamental modes, respectively, as expected from the second term in Eq. (9). This larger splitting for OAM modes is a consequence of the photonic orbit-orbit interaction term being  $l$  times as large as the spin-orbit interaction term. Off-axis twisting therefore lifts the degeneracy of OAM modes with the same TAM, resulting in OAM birefringence. This effect can be used to create OAM-maintaining fibers. Furthermore, twisting can induce coupling between modes, which enables twist-based mode converters [28]. While not explored further in this paper, such a coupling can be observed for the mode pair with a TAM of  $\pm 5$  at a twist rate of  $2.7/\text{mm}$ , explaining the discontinuity in the green curves in Figs. 4(a) and 4(b).

### 4. Fundamental modes in single-mode waveguides

To study single-mode variants of the three waveguide types, the core radius was reduced to  $r_c = 0.2 \mu\text{m}$ , resulting in

a  $V$  number of  $V = 1.92$ . Contrary to the multimode case, the optical properties of these waveguides differ strongly between each other. As the cross section is much narrower, any change in the cross section from a circular profile affects the polarization of the mode as shown in Fig. 5(d). The resulting mix of linear and circular birefringence in the fundamental modes of the helicoidal and Overfelt waveguide can be much larger and of opposite sign than that of the Frenet-Serret waveguide [Fig. 5(b)]. As the cross section of the Frenet-Serret waveguide is circular in the NB plane at all twist rates, its modes remain circularly polarized and their effective indices are accurately described by Eq. (9). Another aspect to consider is that the fraction of power located in air is also dependent on the shape of the cross section. For example, the fraction of power in air is increased at small twist rates ( $\alpha\rho \ll 1$ ) for the Overfelt waveguide and at large twist rates ( $\alpha\rho > 1$ ) for the helicoidal waveguide, which results in a reduction of the effective index (Fig. 5(a) and Fig. S11 of the Supplemental Material [30]). As expected from the analytical formula for the cross sections of the waveguides (Table I), the properties of the Frenet-Serret waveguide converge with those of the helicoidal waveguide for low twist rates and with those of the Overfelt waveguide for high twist rates. The propagation loss of the waveguides will be discussed below in Sec. II G.

## F. Effects of bending on modes in helical waveguides

### 1. Fundamental modes in multimode waveguides

Next, we studied the spatial properties of the modes in more detail with an overview of all modes available in Sec. SX of the Supplemental Material [30]. Regarding the intensity distributions of the fundamental modes in the multimode waveguides, twisting has two effects: (1) the mode profile becomes narrower and (2) it shifts away from the twist axis. These effects are shown in Fig. 6(b) for the Frenet-Serret waveguide and in Fig. S14 for the helicoidal and Overfelt waveguides.

Both effects are well-known from fiber bends in a two-dimensional plane as the radius of curvature decreases [45]. If the bent waveguide is approximated as a circle with a radius of curvature  $R$ , it can be mapped to a straight waveguide

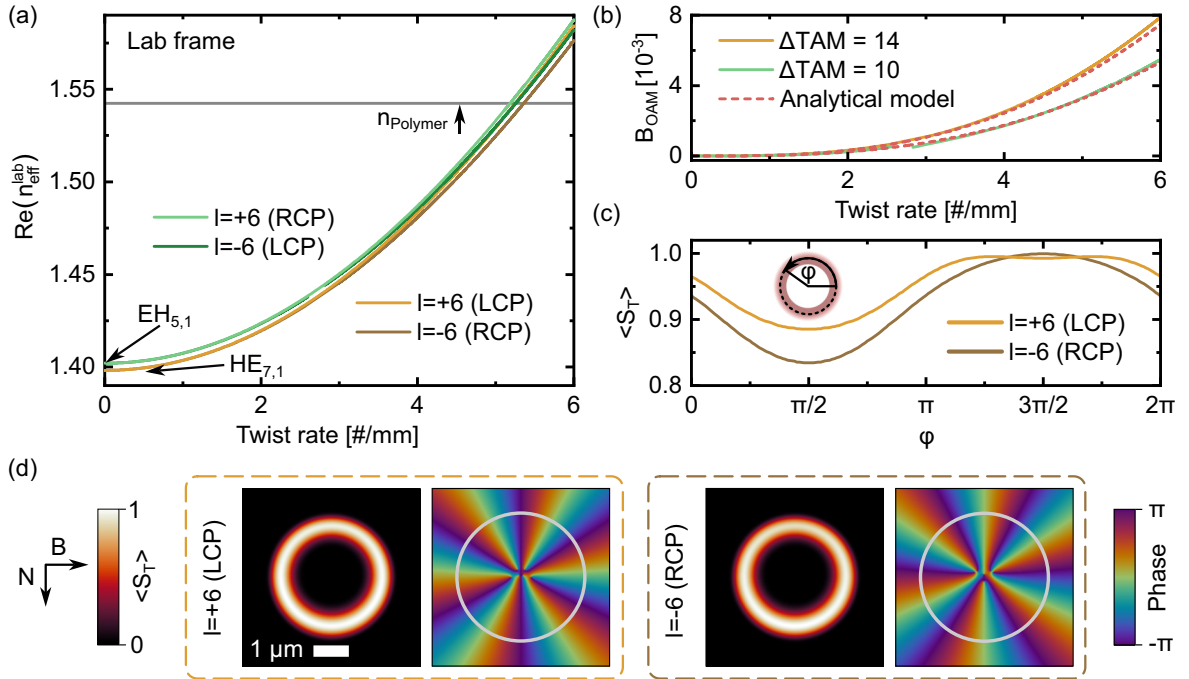


FIG. 4. OAM modes in Frenet-Serret waveguide geometry ( $r_c = 1.8 \mu\text{m}$ ). (a) Twist-rate dependence of the real part of the effective mode index in the laboratory frame for the four modes with  $|l| = 6$ . The two modes with total angular momentum (TAM) of  $\pm 5$  (green) stem from the even and odd  $\text{EH}_{5,1}$  modes of the untwisted waveguide, while the two modes with TAM of  $\pm 7$  (orange) originate in the  $\text{HE}_{7,1}$  modes. (b) OAM birefringence between these mode pairs. Note, that the other pairings ( $+5/-7$  and  $-7/+5$ ) are already nondegenerate in the untwisted case. The simulated splitting matches well with the analytical prediction [red dashed line, Eq. (9)]. (c), (d) Longitudinal component of the Poynting vector of the modes with TAM of  $\pm 7$  for a twist rate of  $5/\text{mm}$ . Evaluating the azimuthal distribution of the Poynting vector along a selected circle shows an increase in the intensity at the side of the waveguide that points towards the central twist axis. This asymmetry is different for the two modes, which might be a result of the photonic orbit-orbit interaction. (d) additionally displays the phase of the B component of the electric field with the cross section of the waveguides shown as gray line.

uide using a conformal transformation [46]. This mapping results in a modified refractive index profile that increases approximately linear (for  $R \gg r_c$ ) across the waveguide and cladding:  $n \approx n_0(1 + x/R)$ , where  $x = 0$  corresponds to the center of the waveguide and  $n_0$  is the refractive index profile of the waveguide before bending [47]. More intuitively, as the mode has to propagate a larger distance on the outside of the bend than on the inside, the mapped refractive index increases away from the center of curvature. The reason for the observed shift of the modal patterns towards the region of higher index can be seen when noting that the scalar wave equation is equivalent to the time-independent Schrödinger equation [48] for a potential equal to  $-n^2$ . Consequently, the mode moves to larger radii to minimize its energy. For helical waveguides, the radius of curvature of the bend is given by  $R = 1/\bar{\kappa}$ , which decreases with increasing twist rate.

## 2. OAM modes in multimode waveguides

While twisting strongly impacts the effective index of OAM modes, its impact on the mode profile is much weaker than for the fundamental mode. Contrary to the fundamental modes, the center of the modes with  $|l| = 6$  does not shift away from the twist axis as shown in Fig. 4(d). This is to be expected since the effect of bending on the mode profile is known to decline as the mode order increases [45,49].

What is typically observed for OAM modes in bent fibers is that the angular intensity distribution is slightly nonuniform with a peak on the side facing away from the center of curvature [45,49,50]. However, the OAM modes in the twisted Frenet-Serret waveguide peak on the side facing towards the twist axis as shown in Fig. 4(c). This asymmetry must, therefore, be purely related to the twist.

## 3. Fundamental modes in single-mode waveguides

The intensity distribution of the modes in the single-mode Frenet-Serret waveguide remains virtually unaffected by twisting due to the confinement provided by the high index contrast as shown in Fig. 7(a) and Fig. S16 of the Supplemental Material [30]. For systems with a lower index contrast, a shift of the center of the mode would be expected [45], similar to what has been discussed above for the multimode system.

## G. Loss in helical waveguides

Propagation loss in off-axis twisted waveguides is different from the loss of the corresponding untwisted waveguide for two reasons: (1) the geometric path length to reach a certain axial distance  $z$  is increased because the light is traveling along a helical trajectory and (2) additional loss arises from bending. The geometric factor effectively increases the intrinsic loss  $\gamma_0$  of the untwisted waveguide, which might be present due to surface roughness or material absorption. We denote the associated attenuation coefficient for the twisted waveguide

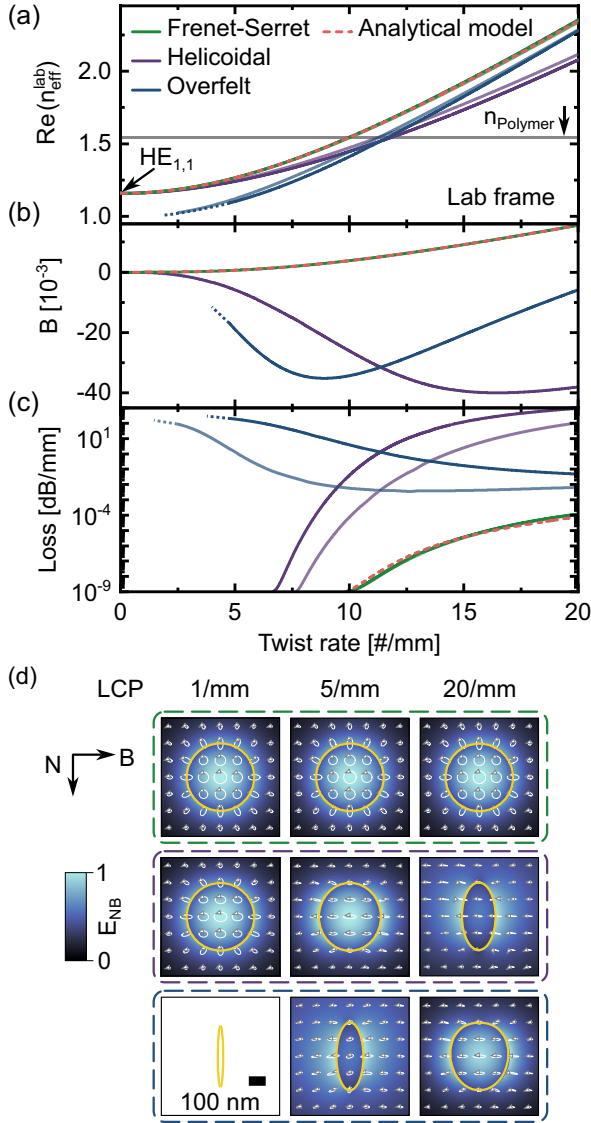


FIG. 5. Optical properties of single-mode helical waveguides ( $r_c = 0.2 \mu\text{m}$ ). (a)–(c) Twist rate dependence of the real part of the effective mode index, the birefringence, and the attenuation of the two fundamental modes calculated in the laboratory frame. A darker color shade denotes the LCP mode, a lighter shade the RCP mode. Red dashed lines in (a)–(c) represent an analytical prediction for the Frenet-Serret waveguide [Eqs. (9) and (12)]. (d) Spatial distribution of the transverse (NB) component of the electric field of the LCP mode at three different twist rates. Polarization ellipses show that the field of the Frenet-Serret waveguide (green box) remains circularly polarized at all twist rates. Helicoidal waveguide (purple box) and Overfelt waveguide (blue box) feature elliptically polarized eigenmodes at high or low twist rates, respectively. The cross section of the waveguides is highlighted as yellow line. Note that the modes of the Overfelt waveguide could not be calculated for twist rates below 5/mm due to very high loss and low confinement in the core [blue dots in (a)–(c) and blank field in (d)].

uide as  $\gamma_{\text{geo}}$  [the attenuation coefficient is generally defined via the relation  $I(z) = I(0) \exp(-\gamma z)$ , where  $I$  denotes the optical power]:

$$\gamma_{\text{geo}} = \gamma_0 \frac{\sqrt{P^2 + (2\pi\rho)^2}}{P} = \gamma_0 \sqrt{1 + \alpha^2 \rho^2}. \quad (11)$$

Bend loss of optical fibers has been studied extensively for situations where the weak guidance approximation is satisfied ( $\Delta \ll 1$ ), the modal field inside the twisted core is the same as in the straight fiber, and the radius of curvature is much larger than the radius of the core ( $R \gg r_c$ ) [51,52]. More advanced models exist if one or more of these assumptions are not satisfied [45,53,54]. Here, we use the model from Ref. [51] that is valid when all three assumptions are met and include a correction factor taking into account that the bends do not lie within a flat plane but occur along a helical path. In this case, the attenuation coefficient  $\gamma_{\text{bend}}$  is given by [29]

$$\gamma_{\text{bend}} = \frac{\sqrt{\pi} V^2 \sqrt{W}}{2r_c U^2} \sqrt{\frac{r_c}{R}} e^{-\frac{4}{3} \frac{R}{r_c} \frac{W^3 \Delta}{V^2}} \times \left( 1 - \frac{1}{2} (\alpha\rho)^2 + \frac{3}{32} (\alpha\rho)^4 \right), \quad (12)$$

correction for helical bend

where  $V = 2\pi(n_{\text{co}}^2 - n_{\text{cl}}^2)r_c/\lambda$  is the  $V$  number,  $\Delta = (n_{\text{co}}^2 - n_{\text{cl}}^2)/(2n_{\text{co}}^2) = 0.29$  is the refractive index contrast, and  $R = 1/\bar{\kappa}$  is the radius of curvature of the helix.  $U(V)$  and  $W(V)$  are numerical solutions to a transcendental equation characterizing the mode and can be obtained from Ref. [51]. For the single-mode Frenet-Serret waveguide, one has  $V = 1.92$ ,  $U = 1.50$ , and  $W = 1.20$  and for its multimode version  $V = 17.25$ ,  $U = 2.27$ , and  $W = 17.10$ . Note that the mode profile of the multimode waveguide changes as the twist rate increases, and thus Eq. (12) is only approximately valid.

The resulting bend loss  $\gamma_{\text{bend}}$  is shown for the Frenet-Serret waveguide in Fig. 5(c), matching well with the simulated data. Interestingly, bending strongly affects the loss of the single-mode waveguide as the twist rate increases while it remains negligibly low for the multimode variant (below  $2 \times 10^{-24}$  dB/mm at the highest investigated twist rate). As the simulated loss of the multimode waveguides is below the noise level of the solver, it is not shown. This difference in bend loss can be understood based on the conformal transformation method described above. Since the mapped refractive index profile increases away from the center of curvature, at some distance from the waveguide—the caustic boundary—the mapped index of the cladding is higher than that of the core mode and the field becomes radiative due to the absence of total internal reflection [47]. As the field of the multimode waveguide remains well confined within the core, its amplitude at the caustic boundary is very low. In the single-mode waveguide on the other hand, a much larger fraction of the field is present inside the cladding, thus explaining the large difference in bend loss.

The geometric contribution to the loss  $\gamma_{\text{geo}}$  was not analyzed in this paper because the material of the waveguide was assumed to be lossless ( $\gamma_0 = 0$ ). Preliminary simulations with lossy materials showed that the total loss is well described as the sum  $\gamma_{\text{geo}} + \gamma_{\text{bend}}$  in this case.

## H. Twist-induced effects on spatial mode properties

### 1. Spin- and OAM-dependent effects

Apart from the large shift of the center of the modes induced by bending, we also observe several spin- and OAM-dependent splittings in the spatial properties of the modes,



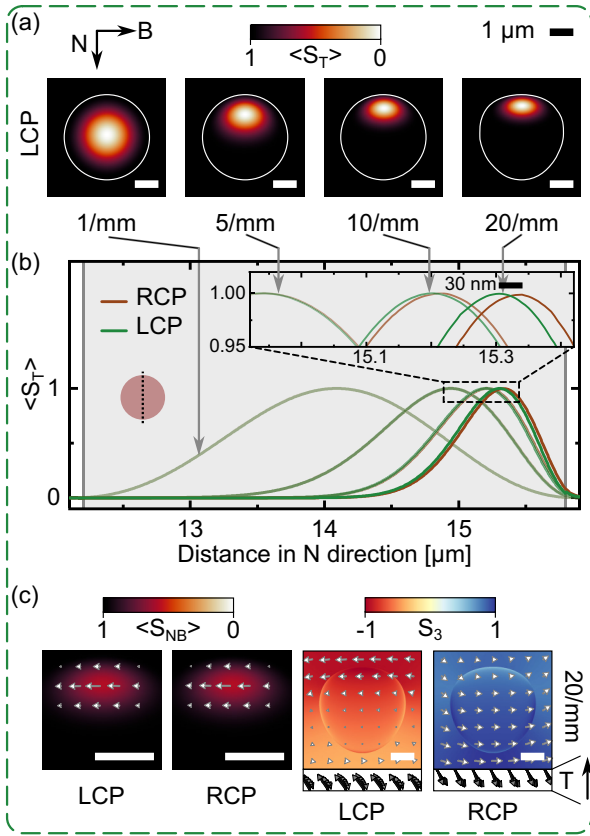


FIG. 6. Spatial properties of modes in the multimode Frenet-Serret waveguide depicted in the TNB frame. (a) Distribution of the T component of the Poynting vector (i.e., tangential to the helix) of the LCP mode at four different twist rates. At increasing twist rate, the waveguide becomes bent such that the center of the mode moves to larger radii, i.e., away from the twist axis. A line cut of these distributions along the N direction through the center of the waveguide is shown in (b). The zoomed inset shows that the RCP mode (brown) moves further outwards than the LCP mode (green), potentially a consequence of the photonic spin Hall effect. (c) At a high twist rate of 20/mm, the Poynting vector develops a transverse component pointing in the negative B direction for both LCP and RCP modes. The spin vector of the electric field  $\mathbf{s}_E$  also develops a transverse component which points in opposite directions for the two polarizations. The magnitude of  $\mathbf{s}_E$  is equal to the third component of the Stokes vector  $S_3$ .

summarized here for the Frenet-Serret waveguide: (1) For the multimode waveguide, the center of the LCP and RCP modes (evaluated on the T component of the Poynting vector) are split along the N direction as shown in Fig. 6(b). The splitting increases with twist rate and reaches 30 nm (about 1% of the core diameter) for a twist rate of 20/mm. (2) In the single-mode case, such a splitting occurs for the transverse component of the Poynting vector  $\mathbf{S}_{NB}$  while no splitting can be observed in its longitudinal component. The splitting reaches 50 nm (12.5% of the core diameter) for a twist rate of 20/mm as shown in Fig. 7(a). (3) For the OAM modes in the multimode variant, we observe that the difference between the intensity on the top and bottom sides of the vortex depends on the sign of the total angular momentum. The bottom and top

refer to the side facing towards and away from the twist axis, respectively, as shown in Fig. 4(c) and 4(d).

As a result, we hypothesize that these spin- and OAM-dependent splittings arise due to an interplay between the confinement provided by the waveguiding structure, and the photonic spin Hall [7,9] and photonic orbital Hall [8,11] effects. When light propagates along a curved trajectory which changes on length scales much larger than the wavelength, its movement can be characterized by equations of motion for the center of gravity of the mode. These equations contain a spin-orbit [5,7] and an orbit-orbit [8] interaction term that results in spatial splittings between modes with distinct total angular momenta as described in more detail in Sec. SIX of the Supplemental Material [30]. In fact, these photonic spin Hall and orbital Hall effects are just another consequence of the spin-orbit and orbit-orbit interaction of light [5], which so accurately describes the circular birefringence of the helical waveguides (cf. Sec. IID). Therefore, it is likely that these effects are at the origin of the observed spatial splitting, although they do not apply directly to modes confined in waveguides.

## 2. Transverse components of the Poynting and spin vectors

At high twist rates ( $> 10/\text{mm}$ ), the fundamental modes of all investigated waveguide types (single-mode and multimode) develop an increasingly large transverse component of the Poynting vector  $\mathbf{S}_{NB}$ , shown exemplarily for the Frenet-Serret waveguide in Figs. 6(c) and 7(a). The direction of this additional component is along the negative B direction regardless of polarization. Similarly, the spin vector  $\mathbf{s}_E$  of the electric field contains a transverse component along the B direction for high twist rates, pointing in opposite directions for the two spin states. The evolution of these properties at different twist rates can be found for all waveguide types in Sec. SX of the Supplemental Material [30]. Transverse spin is well-known to occur in evanescent waves where its direction is independent of polarization and led to applications involving spin-momentum locking [55–57]. The origin of transverse spin and momentum in helical waveguides remains to be studied.

## 3. Elliptically polarized eigenmodes and superchiral fields in helicoidal waveguides

Lastly, we want to point out an effect that becomes apparent when the cross section of the twisted single-mode waveguide is elliptical in the NB plane as is the case for the helicoidal waveguide. As discussed, the interplay of the linear birefringence of the core and the circular birefringence caused by the twist results in elliptically polarized eigenmodes. Similar to a linearly polarized mode, the modal fields are enhanced in the direction of the long axis of the polarization ellipse. These locations differ for the electric and magnetic field as shown in Fig. 7(b). In this example, the magnetic field is enhanced at the top and bottom surface of the core, while the electric field is reduced. Combined with the fact that the fields are still circularly polarized to a sufficient degree, such a configuration is ideal for creating superchiral fields. We quantify the superchirality in terms of the factor  $g_{\text{field}}$  (defined and explained in Sec. SVIII of the Supplemental Material [30]), with  $|g_{\text{field}}| > n$  indicating a superchiral field. In brief,  $g_{\text{field}}$

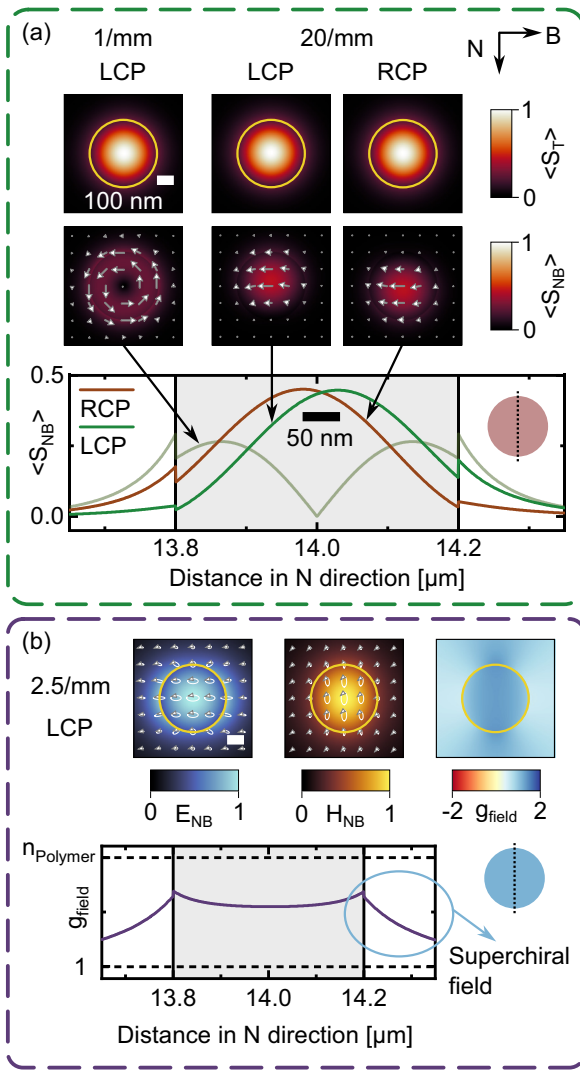


FIG. 7. Spatial properties of modes in two single-mode helical waveguide geometries ( $r_c = 0.2 \mu\text{m}$ ). (a) Distribution of the longitudinal (T) and transverse (NB) component of the Poynting vector at low (1/mm) and high (20/mm) twist rates for the Frenet-Serret waveguide. The longitudinal component remains unchanged when the twist rate increases while the transverse component shifts in opposite directions along the N axis. This splitting might be a consequence of the photonic spin Hall effect. (b) The elliptically polarized eigenmodes of the helicoidal waveguide feature a reduced electric field (left panel) on the top and bottom surface of the waveguide while the magnetic field is enhanced (middle panel). This difference results in a superchiral field with  $g_{\text{field}}$  being larger than the refractive index on the outside of the core (right panel). A line cut of this distribution along the N direction through the center of the waveguide is shown in the bottom panel. The yellow circles in (a) and (b) highlight the cross section of the waveguides.

is the enhancement factor of the molecular  $g$ -factor, which is typically measured in chiral sensing experiments. Here, we found an enhancement factor of  $\approx 1.4$  on the surface of the waveguide. Values of  $g_{\text{field}}$  for other twist rates can be found in Fig. S12 of the Supplemental Material [30]. We note that this value is lower than in the pioneering experiment for superchiral fields, where an enhancement of around 11

was measured [31,32]. However, our enhancement occurs in a region of space where the field has an appreciable intensity while the pioneering experiment was carried out in the node of a standing wave where the intensity is low. Further research is required to optimize the superchirality in helical waveguides (e.g., by increasing both the twist rate and the linear birefringence), and to find a method to place molecules precisely in the regions of superchiral field.

### III. DISCUSSION

The numerical results for the effective index of all three multimode helical waveguides are in high agreement with the analytical prediction, underpinning the fact that the cause of the circular birefringence and OAM birefringence is a purely geometrical effect inherent to the helical path. As such, the phase difference between modes with different TAM  $\delta n_{\text{eff}}^{\text{lab}} k_{0z}$  does not depend on wavelength, material, and core size [cf. Eq. (9)]. Helical waveguides can therefore find applications as broadband spin- and OAM-preserving waveguides. More generally, any waveguide with nonzero torsion at each point of its trajectory will be able to preserve the angular momentum state of the light.

A typical example of a Frenet-Serret waveguide is a piece of fiber helically coiled around a cylinder, as it used in the initial experiments on helical waveguides [1,3,14,39]. Helical waveguides can also be created by twisting a fiber with an off-axis core [2,17]. Such fibers are fabricated by either spinning the preform while drawing the fiber or in a thermal post-processing step [36]. In this situation, it is conceivable that both helicoidal or Frenet-Serret type waveguides can, in principle, be created depending on the fabrication conditions. Since both types converge to the same shape at low twist rates ( $\alpha\rho \gg 1$ ), which have not yet been experimentally realized (see Table SI of the Supplemental Material [30]). Finally, the Overfelt waveguide might be relevant for situations where a helical waveguide is constructed by extending a toroidal shape in the  $z$  direction or to describe Frenet-Serret waveguides at large twist rates.

All waveguides created with planar fabrication techniques, on the other hand, necessarily have zero torsion and can therefore not exhibit circular or OAM birefringence based on geometric effects. To realize complex 3D waveguides directly on-chip, 3D nanoprinting via two-photon-polymerization has emerged over the last decade as a promising alternative to planar fabrication techniques [33,58,59]. This technique can be used to realize all three helical waveguide types discussed in this paper and provides the ability to freely choose the cross section within the NB plane. While the twist rate achievable in fibers is inherently limited by the properties of the glass, 3D nanoprinting can potentially realize higher twist rates with pitch distances down to the core diameter. Here, we explored waveguides with pitch distances as low as 14 times the core diameter, but even lower pitch distances seem theoretically feasible given the low bend loss in the multimode versions of the waveguides. Preliminary experiments showed that twist rates of 10/mm can be reached experimentally, corresponding to  $\alpha\rho = 0.9$  while a value of  $\alpha\rho \approx 0.5$  was reported for a different design in Ref. [33]. Another technique that allows

realizing helical waveguides on a chip is direct laser writing, where a small refractive index modification is created in glass by scanning of a focused femtosecond laser beam [60–62]. However, precise control over the cross section of the waveguide proved to be challenging due to aberrations of the focal spot inside the glass that need to be compensated [63,64].

The study of the polarization properties of modes in helical waveguides revealed that the shape of the cross section in the NB plane strongly impacts their optical properties if the waveguides are single mode. Any deviation from a circular cross section can induce linear birefringence, thus creating elliptically polarized eigenmodes. The simple analytical formula by Alexeyev and Yavorsky [28] is therefore not sufficient to describe the effective index in this specific case. Instead, a recently developed theoretical model for off-axis twisted waveguides with elliptical cross sections in the Frenet-Serret frame [35] could be applied to predict the birefringence and polarization of the helicoidal and Overfelt waveguide. This would require prior knowledge of the modes of an untwisted waveguide with the same elliptical cross section. Additionally, a recent perturbative model studied the evolution of polarization in a helical waveguide when excited by the fundamental mode of a straight waveguide, which corresponds to the typical situation in experiments [65].

Elliptically polarized eigenmodes also occur in on-axis twisted waveguides with an elliptical cross section and were applied in creating ultranarrow (sub-megahertz) spectral dips in stimulated Brillouin scattering [66]. The authors used that the polarization state of elliptically polarized modes depends on the wavelength, which is another intriguing effect that is unique to twisted waveguides.

#### IV. CONCLUSION

Using comprehensive theoretical and numerical analysis, we revealed the differences between three common helical waveguide geometries, which naturally result from the use of the Frenet-Serret, helicoidal, or Overfelt frame. While the Frenet-Serret waveguide maintains a circular cross section in the NB plane at all twist rates, the helicoidal and Overfelt waveguides can exhibit elliptical cross sections, leading to noncircular polarization if the core size is small. Such elliptically polarized modes were found to generate superchiral fields on the surface of the waveguides. Conversely, the effective index of all circularly polarized waveguide modes can be accurately described by an analytical formula by Alexeyev and Yavorsky [28] [Eq. (9)] even if (1) the index contrast is large ( $n = 1.54$  to air,  $\Delta = 0.29$ ), (2) the mode is not entirely transversely polarized, (3) the mode profile is different from that of the untwisted waveguide, and (4) the twist rate ap-

proaches relatively high values. Propagation loss was found to consist of bend loss [29] and intrinsic loss.

Additionally, we derived a transformation of the effective index from the helicoidal to the laboratory frame applicable to both on- and off-axis twisted waveguides up to arbitrary twist rates. We note that such a transformation should not be performed if the modes are elliptically polarized. Lastly, the study explored spin- and OAM-dependent splittings in the spatial intensity distribution of the modes, suggesting links to the photonic spin Hall and orbital Hall effects.

Traditionally, helical waveguides were realized by twisting glass fibers, limiting the achievable twist rates and lacking precise control over waveguide cross section. However, emerging fabrication techniques such as 3D nanoprinting [33,41,43] or direct laser writing hold promise for overcoming these limitations and enabling further chip-integrated applications of helical waveguides, including chiral spectroscopy, integrated Brillouin lasing for ultrahigh-resolution optical sensing [66] and OAM-maintaining transport of optical signals. On a fundamental level, exploring ultrahigh twist rates with pitch distances close to the diameter of the off-axis core may offer insights into complex physical effects such as strong spin-orbit and orbit-orbit interactions.

#### ACKNOWLEDGMENTS

We thank A. Lorenz (IPHT Jena) for helpful discussion on bending effects in fibers. Furthermore, we thank S. Burger and M. Hammerschmidt (JCMwave GmbH) for quickly patching an error in JCMwave that affected the calculation of fields at high twist rates. The authors acknowledge financial support from the German Research Foundation via Grants No. MA 4699/2-1, No. MA 4699/9-1, No. SCHM2655/11-1, No. SCHM2655/15-1, No. SCHM2655/8-1, No. SCHM2655/22-1, and No. WE 5815/5-1. S.A.M. additionally acknowledges the Lee-Lucas Chair in Physics.

#### APPENDIX: NUMERICAL SIMULATIONS

All waveguides were simulated in the helicoidal coordinate system using a commercial FEM solver (PropagatingMode module of JCMwave). The waveguide core is surrounded by air, followed by a PML to absorb outgoing power resulting from bending of the waveguide. The helicoidal coordinate system is natively supported by the solver, including an appropriate definition of the PML. Convergence of the solver in terms of mesh size in core and air regions, and the distance between the waveguide and PML has been checked.

- 
- [1] J. N. Ross, The rotation of the polarization in low birefringence monomode optical fibres due to geometric effects, *Opt. Quantum Electron.* **16**, 455 (1984).  
 [2] M. P. Varnham, Helical core circularly-birefringent fibers, Proc. IOOC-ECOC (Venice), 135 (1985).  
 [3] J. Qian and C. D. Hussey, Circular birefringence in helical-core fibre, *Electron. Lett.* **22**, 515 (1986).

- [4] M. V. Berry, Interpreting the anholonomy of coiled light, *Nature (London)* **326**, 277 (1987).  
 [5] K. Y. Bliokh, F. J. Rodríguez-Fortuño, F. Nori, and A. V. Zayats, Spin-orbit interactions of light, *Nat. Photonics* **9**, 796 (2015).  
 [6] *Elementary Differential Geometry*, 2nd ed., edited by B. O'Neill (Academic Press, Boston, 2006).

- [7] V. S. Liberman and B. Ya. Zel'dovich, Spin-orbit interaction of a photon in an inhomogeneous medium, *Phys. Rev. A* **46**, 5199 (1992).
- [8] K. Y. Bliokh, Geometrical optics of beams with vortices: Berry phase and orbital angular momentum Hall effect, *Phys. Rev. Lett.* **97**, 043901 (2006).
- [9] K. Y. Bliokh, A. Niv, V. Kleiner, and E. Hasman, Geometrodynamics of spinning light, *Nat. Photonics* **2**, 748 (2008).
- [10] K. Yu. Bliokh and Yu. P. Bliokh, Topological spin transport of photons: The optical Magnus effect and Berry phase, *Phys. Lett. A* **333**, 181 (2004).
- [11] V. G. Fedoseyev, Spin-independent transverse shift of the centre of gravity of a reflected and of a refracted light beam, *Opt. Commun.* **193**, 9 (2001).
- [12] S. C. Rashleigh and R. Ulrich, Magneto-optic current sensing with birefringent fibers, *Appl. Phys. Lett.* **34**, 768 (1979).
- [13] R. Ulrich and A. Simon, Polarization optics of twisted single-mode fibers, *Appl. Opt.* **18**, 2241 (1979).
- [14] A. M. Smith, Polarization and magneto-optic properties of single-mode optical fiber, *Appl. Opt.* **17**, 52 (1978).
- [15] G. K. L. Wong, M. S. Kang, H. W. Lee, F. Biancalana, C. Conti, T. Weiss, and P. St. J. Russell, Excitation of orbital angular momentum resonances in helically twisted photonic crystal fiber, *Science* **337**, 446 (2012).
- [16] P. Roth, Y. Chen, M. C. Günendi, R. Beravat, N. N. Edavalath, M. H. Frosz, G. Ahmed, G. K. L. Wong, and P. St. J. Russell, Strong circular dichroism for the  $HE_{11}$  mode in twisted single-ring hollow-core photonic crystal fiber, *Optica* **5**, 1315 (2018).
- [17] X. Ma, C.-H. Liu, G. Chang, and A. Galvanauskas, Angular-momentum coupled optical waves in chirally-coupled-core fibers, *Opt. Express* **19**, 26515 (2011).
- [18] X. Xi, G. K. L. Wong, T. Weiss, and P. St. J. Russell, Measuring mechanical strain and twist using helical photonic crystal fiber, *Opt. Lett.* **38**, 5401 (2013).
- [19] X. M. Xi, G. K. L. Wong, M. H. Frosz, F. Babic, G. Ahmed, X. Jiang, T. G. Euser, and P. St. J. Russell, Orbital-angular-momentum-preserving helical Bloch modes in twisted photonic crystal fiber, *Optica* **1**, 165 (2014).
- [20] P. L. Overfelt, Helical localized wave solutions of the scalar wave equation, *J. Opt. Soc. Am. A* **18**, 1905 (2001).
- [21] V. I. Kopp, V. M. Churikov, J. Singer, N. Chao, D. Neugroschl, and A. Z. Genack, Chiral fiber gratings, *Science* **305**, 74 (2004).
- [22] S. Oh, K. R. Lee, U.-C. Paek, and Y. Chung, Fabrication of helical long-period fiber gratings by use of a  $CO_2$  laser, *Opt. Lett.* **29**, 1464 (2004).
- [23] H. Xu and L. Yang, Conversion of orbital angular momentum of light in chiral fiber gratings, *Opt. Lett.* **38**, 1978 (2013).
- [24] K. Ren, L. Ren, J. Liang, L. Yang, J. Xu, D. Han, Y. Wang, J. Liu, J. Dong, H. He, and W. Zhang, Excitation of high-quality orbital angular momentum vortex beams in an adiabatically helical-twisted single-mode fiber, *Opt. Express* **29**, 8441 (2021).
- [25] J. F. Bauters, M. J. R. Heck, D. D. John, J. S. Barton, C. M. Bruinink, A. Leinse, R. G. Heideman, D. J. Blumenthal, and J. E. Bowers, Planar waveguides with less than 0.1 dB/m propagation loss fabricated with wafer bonding, *Opt. Express* **19**, 24090 (2011).
- [26] D. Dai, J. Bauters, and J. E. Bowers, Passive technologies for future large-scale photonic integrated circuits on silicon: Polarization handling, light non-reciprocity and loss reduction, *Light: Sci. Appl.* **1**, e1 (2012).
- [27] H. Lee, T. Chen, J. Li, O. Painter, and K. J. Vahala, Ultra-low-loss optical delay line on a silicon chip, *Nat. Commun.* **3**, 867 (2012).
- [28] C. N. Alexeyev and M. A. Yavorsky, Generation and conversion of optical vortices in long-period helical core optical fibers, *Phys. Rev. A* **78**, 043828 (2008).
- [29] D. B. S. Soh, J. Nilsson, J. K. Sahu, and L. J. Cooper, Geometrical factor modification of helical-core fiber radiation loss formula, *Opt. Commun.* **222**, 235 (2003).
- [30] See Supplemental Material at <http://link.aps.org/supplemental/10.1103/PhysRevB.109.165301> for an overview of works on off-axis twisted waveguides, detailed derivations of all presented results, and further simulation results, which includes Refs. [67–84].
- [31] Y. Tang and A. E. Cohen, Optical chirality and its interaction with matter, *Phys. Rev. Lett.* **104**, 163901 (2010).
- [32] Y. Tang and A. E. Cohen, Enhanced enantioselectivity in excitation of chiral molecules by superchiral light, *Science* **332**, 333 (2011).
- [33] H. Gao, G. F. R. Chen, P. Xing, J. W. Choi, H. Y. Low, and D. T. H. Tan, High-resolution 3D printed photonic waveguide devices, *Adv. Opt. Mater.* **8**, 2000613 (2020).
- [34] W. Kühnel, *Differential Geometry: Curves, Surfaces, Manifolds*, 3rd ed. (American Mathematical Society, Providence, Rhode Island, 2015).
- [35] Y. Chen and P. St. J. Russell, Frenet–Serret analysis of helical Bloch modes in  $N$ -fold rotationally symmetric rings of coupled spiraling optical waveguides, *J. Opt. Soc. Am. B* **38**, 1173 (2021).
- [36] P. St. J. Russell, R. Beravat, and G. K. L. Wong, Helically twisted photonic crystal fibres, *Philos. Trans. R. Soc. A* **375**, 20150440 (2017).
- [37] T. Weiss, G. K. L. Wong, F. Biancalana, S. M. Barnett, X. M. Xi, and P. St. J. Russell, Topological Zeeman effect and circular birefringence in twisted photonic crystal fibers, *J. Opt. Soc. Am. B* **30**, 2921 (2013).
- [38] R. Y. Chiao and Y.-S. Wu, Manifestations of Berry's topological phase for the photon, *Phys. Rev. Lett.* **57**, 933 (1986).
- [39] A. Tomita and R. Y. Chiao, Observation of Berry's topological phase by use of an optical fiber, *Phys. Rev. Lett.* **57**, 937 (1986).
- [40] M. V. Berry, Quantal phase factors accompanying adiabatic changes, *Proc. R. Soc. London, Ser. A* **392**, 45 (1984).
- [41] C. Jain, A. Braun, J. Gargiulo, B. Jang, G. Li, H. Lehmann, S. A. Maier, and M. A. Schmidt, Hollow core light cage: Trapping light behind bars, *ACS Photonics* **6**, 649 (2019).
- [42] J. Bürger, J. Kim, B. Jang, J. Gargiulo, M. A. Schmidt, and S. A. Maier, Ultrahigh-aspect-ratio light cages: Fabrication limits and tolerances of free-standing 3D nanoprinted waveguides, *Opt. Mater. Express* **11**, 1046 (2021).
- [43] J. Bürger, V. Schalles, J. Kim, B. Jang, M. Zeisberger, J. Gargiulo, L. de S. Menezes, M. A. Schmidt, and S. A. Maier, 3D-nanoprinted antiresonant hollow-core microgap waveguide: An on-chip platform for integrated photonic devices and sensors, *ACS Photonics* **9**, 3012 (2022).

- [44] S. Ramachandran and P. Kristensen, Optical vortices in fiber, *Nanophotonics* **2**, 455 (2013).
- [45] D. Marcuse, Field deformation and loss caused by curvature of optical fibers, *J. Opt. Soc. Am.* **66**, 311 (1976).
- [46] M. Heiblum and J. Harris, Analysis of curved optical waveguides by conformal transformation, *IEEE J. Quantum Electron.* **11**, 75 (1975).
- [47] R. T. Schermer and J. H. Cole, Improved bend loss formula verified for optical fiber by simulation and experiment, *IEEE J. Quantum Electron.* **43**, 899 (2007).
- [48] D. J. Griffiths and D. F. Schroeter, *Introduction to Quantum Mechanics*, 3rd ed. (Cambridge University Press, Cambridge, UK, 2018).
- [49] X. Jiao, H. Zhang, X. Zhang, H. Li, J. Wei, Z. Wang, L. Xi, W. Zhang, and X. Tang, Performance of circular photonic crystal fiber transmitting orbital angular momentum modes under macro-bending, *J. Opt.* **21**, 065703 (2019).
- [50] H. Yan, S. Li, Z. Xie, X. Zheng, C. Du, H. Zhang, and B. Zhou, Deformation of orbital angular momentum modes in bending ring-core fiber, *Chin. Opt. Lett.* **15**, 030501 (2017).
- [51] A. W. Snyder and J. D. Love, *Optical Waveguide Theory* (Chapman and Hall, New York, 1983).
- [52] D. Marcuse, Curvature loss formula for optical fibers, *J. Opt. Soc. Am.* **66**, 216 (1976).
- [53] E. A. J. Marcatili, Bends in optical dielectric guides, *Bell Syst. Tech. J.* **48**, 2103 (1969).
- [54] R. W. Smink, B. P. De Hon, and A. G. Tjihuis, Bending loss in optical fibers—a full-wave approach, *J. Opt. Soc. Am. B* **24**, 2610 (2007).
- [55] K. Y. Bliokh, A. Y. Bekshaev, and F. Nori, Extraordinary momentum and spin in evanescent waves, *Nat. Commun.* **5**, 3300 (2014).
- [56] A. Aiello, P. Banzer, M. Neugebauer, and G. Leuchs, From transverse angular momentum to photonic wheels, *Nat. Photonics* **9**, 789 (2015).
- [57] P. Lodahl, S. Mahmoodian, S. Stobbe, A. Rauschenbeutel, P. Schneeweiss, J. Volz, H. Pichler, and P. Zoller, Chiral quantum optics, *Nature (London)* **541**, 473 (2017).
- [58] N. Lindenmann, G. Balthasar, D. Hillerkuss, R. Schmogrow, M. Jordan, J. Leuthold, W. Freude, and C. Koos, Photonic wire bonding: A novel concept for chip-scale interconnects, *Opt. Express* **20**, 17667 (2012).
- [59] M. Schumann, T. Bückmann, N. Gruhler, M. Wegener, and W. Pernice, Hybrid 2D–3D optical devices for integrated optics by direct laser writing, *Light Sci. Appl.* **3**, e175 (2014).
- [60] M. C. Rechtsman, J. M. Zeuner, Y. Plotnik, Y. Lumer, D. Podolsky, F. Dreisow, S. Nolte, M. Segev, and A. Szameit, Photonic floquet topological insulators, *Nature (London)* **496**, 196 (2013).
- [61] A. Szameit and S. Nolte, Discrete optics in femtosecond-laser-written photonic structures, *J. Phys. B: At. Mol. Opt. Phys.* **43**, 163001 (2010).
- [62] S. Gross and M. J. Withford, Ultrafast-laser-inscribed 3D integrated photonics: Challenges and emerging applications, *Nanophotonics* **4**, 332 (2015).
- [63] P. S. Salter, A. Jesacher, J. B. Spring, B. J. Metcalf, N. Thomas-Peter, R. D. Simmonds, N. K. Langford, I. A. Walmsley, and M. J. Booth, Adaptive slit beam shaping for direct laser written waveguides, *Opt. Lett.* **37**, 470 (2012).
- [64] P. S. Salter and M. J. Booth, Adaptive optics in laser processing, *Light: Sci. Appl.* **8**, 110 (2019).
- [65] T. B. Mieling and M. A. Oancea, Polarization transport in optical fibers beyond Rytov’s law, *Phys. Rev. Res.* **5**, 023140 (2023).
- [66] N. Choksi, Y. Liu, R. Ghasemi, and L. Qian, Sub-megahertz spectral dip in a resonator-free twisted gain medium, *Nat. Photonics* **16**, 498 (2022).
- [67] S. Stützer, Y. Plotnik, Y. Lumer, P. Titum, N. H. Lindner, M. Segev, M. C. Rechtsman, and A. Szameit, Photonic topological Anderson insulators, *Nature (London)* **560**, 461 (2018).
- [68] R. P. Feynman, R. B. Leighton, and M. L. Sands, *The Feynman Lectures on Physics*, new millennium ed. (Basic Books, New York, 2011).
- [69] P. Roth, G. K. L. Wong, M. H. Frosz, G. Ahmed, and P. St. J. Russell, Full-field characterization of helical Bloch modes guided in twisted coreless photonic crystal fiber, *Opt. Lett.* **44**, 5049 (2019).
- [70] X. Zeng, P. St. J. Russell, C. Wolff, M. H. Frosz, G. K. L. Wong, and B. Stiller, Nonreciprocal vortex isolator via topology-selective stimulated Brillouin scattering, *Sci. Adv.* **8**, eabq6064 (2022).
- [71] M. Born and E. Wolf, *Principles of Optics: 60th Anniversary Edition*, 7th ed. (Cambridge University Press, Cambridge, UK, 2019).
- [72] R. Beravat, G. K. L. Wong, M. H. Frosz, X. M. Xi, and P. St. J. Russell, Twist-induced guidance in coreless photonic crystal fiber: A helical channel for light, *Sci. Adv.* **2**, e1601421 (2016).
- [73] G. K. L. Wong, X. M. Xi, M. H. Frosz, and P. St. J. Russell, Enhanced optical activity and circular dichroism in twisted photonic crystal fiber, *Opt. Lett.* **40**, 4639 (2015).
- [74] N. N. Edavalath, M. C. Günendi, R. Beravat, G. K. L. Wong, M. H. Frosz, J.-M. Ménard, and P. St. J. Russell, Higher-order mode suppression in twisted single-ring hollow-core photonic crystal fibers, *Opt. Lett.* **42**, 2074 (2017).
- [75] L. D. Barron, *Molecular Light Scattering and Optical Activity*, 2nd ed. (Cambridge University Press, Cambridge, UK, 2004).
- [76] L. Allen, M. W. Beijersbergen, R. J. C. Spreeuw, and J. P. Woerdman, Orbital angular momentum of light and the transformation of Laguerre-Gaussian laser modes, *Phys. Rev. A* **45**, 8185 (1992).
- [77] J. J. Gil, A. T. Friberg, A. Norrman, and T. Setälä, Effect of polarimetric nonregularity on the spin of three-dimensional polarization states, *New J. Phys.* **23**, 063059 (2021).
- [78] L. Marrucci, C. Manzo, and D. Paparo, Optical spin-to-orbital angular momentum conversion in inhomogeneous anisotropic media, *Phys. Rev. Lett.* **96**, 163905 (2006).
- [79] K. Okamoto, *Fundamentals of Optical Waveguides*, 2nd ed. (Elsevier, Amsterdam, Boston, 2006).
- [80] S. Loranger, Y. Chen, P. Roth, M. H. Frosz, G. K. L. Wong, and P. St. J. Russell, Bragg reflection and conversion between helical Bloch modes in chiral three-core photonic crystal fiber, *J. Lightwave Technol.* **38**, 4100 (2020).
- [81] Y. K. Kato, R. C. Myers, A. C. Gossard, and D. D. Awschalom, Observation of the spin Hall effect in semiconductors, *Science* **306**, 1910 (2004).

- [82] V. I. Kopp, V. M. Churikov, J. Singer, D. Neugroschl, and A. Z. Genack, Chiral fiber sensors, *Proc. SPIE* **7677**, 76770U (2010).
- [83] J. Wunderlich, B. Kaestner, J. Sinova, and T. Jungwirth, Experimental observation of the spin-Hall effect in a two-dimensional spin-orbit coupled semiconductor system, *Phys. Rev. Lett.* **94**, 047204 (2005).
- [84] X. M. Xi, T. Weiss, G. K. L. Wong, F. Biancalana, S. M. Barnett, M. J. Padgett, and P. St. J. Russell, Optical activity in twisted solid-core photonic crystal fibers, *Phys. Rev. Lett.* **110**, 143903 (2013).